





Article

Satellite-Derived Bathymetry for Selected Shallow Maltese Coastal Zones

Gareth Darmanin , Adam Gauci , Alan Deidun, Luciano Galone  and Sebastiano D'Amico * 

Department of Geosciences, University of Malta, MSD2080 Msida, Malta; gareth.darmanin@um.edu.mt (G.D.); adam.gauci@um.edu.mt (A.G.); alan.deidun@um.edu.mt (A.D.); luciano.galone@um.edu.mt (L.G.)

* Correspondence: sebastiano.damico@um.edu.mt

Featured Application: The main outcome and procedure described in this paper aim to equip Public Administrations with a tool that can provide on-demand support.

Abstract: Bathymetric information has become essential to help maintain and operate coastal zones. Traditional in situ bathymetry mapping using echo sounders is inefficient in shallow waters and operates at a high logistical cost. On the other hand, lidar mapping provides an efficient means of mapping coastal areas. However, this comes at a high acquisition cost as well. In comparison, satellite-derived bathymetry (SDB) provides a more cost-effective way of mapping coastal regions, albeit at a lower resolution. This work utilises all three of these methods collectively, to obtain accurate bathymetric depth data of two pocket beaches, Golden Bay and Ġhajn Tuffieħa, located in the northwestern region of Malta. Using the Google Earth Engine platform, together with Sentinel-2 data and collected in situ measurements, an empirical pre-processing workflow for estimating SDB was developed. Four different machine learning algorithms which produced differing depth accuracies by calibrating SDBs with those derived from alternative techniques were tested. Thus, this study provides an insight into the depth accuracy that can be achieved for shallow coastal regions using SDB techniques.

Keywords: bathymetry; ocean remote sensing; satellite-derived bathymetry; Maltese islands



Citation: Darmanin, G.; Gauci, A.; Deidun, A.; Galone, L.; D'Amico, S. Satellite-Derived Bathymetry for Selected Shallow Maltese Coastal Zones. *Appl. Sci.* **2023**, *13*, 5238. <https://doi.org/10.3390/app13095238>

Academic Editor: Atsushi Mase

Received: 10 March 2023

Revised: 4 April 2023

Accepted: 6 April 2023

Published: 22 April 2023



Copyright: © 2023 by the authors. Licensee MDPI, Basel, Switzerland. This article is an open access article distributed under the terms and conditions of the Creative Commons Attribution (CC BY) license (<https://creativecommons.org/licenses/by/4.0/>).

1. Introduction

Bathymetry is the key parameter that provides the depth difference between the sea surface and the sea floor [1] and provides means of quantifying the depths of multiple water bodies including oceans, rivers, seas, streams, and lakes [2]. Furthermore, bathymetry encompasses a similar geospatial framework to land topography, embodying critical boundary conditions for oceanographic, geological, biological, and geophysical systems [3]. Accurate determination of the water depth has become crucial in understanding several global interaction processes which in turn influence a number of marine factors including, but not solely, the flow of sea water carrying heat, pollutants, nutrients, and salt [4]. High resolution bathymetric data are crucial for various purposes including monitoring underwater topography, generating nautical charts to aid in navigation, and gauging the movement of deposited sediment underwater [5,6]. Additionally, in relation to ongoing worldwide effects on our environment, bathymetric information has become ever more important to understand the effect that climate change is inducing on the marine environment, to detect sea-level rise and underwater subsidence, and to notify scientists of any changes experienced by coastal morphodynamics [7].

Bathymetric information is paramount to help maintain and operate coastal zones. These transitional, dynamic, and rapidly changing regions between land and water incorporate significant economic, social, and biological value which experience various pressures resulting from both natural and anthropogenic processes [8,9]. Understanding

the submerged topography helps in achieving a number of marine related applications, for instance, realistic hydrodynamic 3D modelling, exploration of submerged landscapes and archaeological sites, coastal climate assessments [10], and port and waterway dredging, as well as resource management [11]. Bathymetry is at the forefront of coastal modelling, and thus, the availability of comprehensive depth information at various temporal and spatial scales is fundamental [12].

Acoustically driven technologies and airborne laser techniques are amongst the most conventional methods used to conduct in situ bathymetric surveys. The two most widely adopted acoustic methods for vessel-based high-resolution mapping of coastal regions are Singlebeam (SBES) and Multibeam Echo Sounders (MBES) [13]. Sound navigation and ranging (Sonar) bathymetry techniques produce highly precise depth values in deeper waters. Despite that, acoustic techniques encounter difficulties and lose efficacy in shallower environments with depths measuring only a few tenths of a metre [14]. Moreover, there are certain remote and constantly changing coastal areas that cannot be reached by hydrographic vessels, leading to insufficient and outdated data in those particular locations [15]. Thus, under these circumstances, bathymetric data are gathered utilising airborne light detection and ranging (lidar) techniques [16]. While lidar bathymetric mapping has the potential to deliver precise results at a centimetre scale, it is constrained by spatial coverage limitations, restricted only to small regions as a result of technical barriers [17]. Regardless of the fact that these methods can generate precise water depth data, they are associated with substantial expenses and logistical challenges that often impede the collection of adequate coastal bathymetric data [18].

Presently, the collection of bathymetric data is being conducted via satellites equipped with optical sensors that utilise multi-spectral and hyper-spectral technology [19]. Multi-spectral satellites provide an alternative method for gathering shallow coastal water depth data by virtue of their wide swath width that enables them to provide information at different spatial and temporal scales in a cost-effective manner [20]. Furthermore, SDB holds significant value for researchers, particularly in remote regions of the world where in situ measurements are challenging or unfeasible [1]. Therefore, despite having a lower resolution, SDB mitigates the limitations inherent by the conventional in situ acoustic and optical methods [21].

Recent technological developments in SDB provide opportunities for new methodologies that can reveal the bathymetry of uncharted coastal areas and facilitate the investigation of seabed morphology changes. In Europe, bathymetric data are either considerably antiquated or not accessible [9]. Hence, modern techniques that integrate both in situ data and satellite-derived imagery can aid in the comprehensive mapping of the shallow coastal characteristics in Europe [22]. The primary objective of the current study is to compute the bathymetry of two coastal regions in the Maltese Islands through the utilisation of remote sensing satellite data, together with in situ lidar and sonar technologies.

The Maltese Islands are located in the centre of the Mediterranean Sea between Sicily and the North African coast and are made up of three principal islands, Malta, Gozo, and Comino together with a number of islets and rocks, having a total land surface area of 316.75 square kilometres [23]. The Maltese archipelago straddles the northern rim of the Pantelleria rift, a graben system that has been active since the late Miocene up to present times, traversing the wide shelf platform connecting Europe and Africa [24]. The bathymetry bordering the eastern flank of the Maltese Islands is composed of a wide planar continental shelf, bounded by a linear escarpment aligned parallel to the coast. On the other hand, the western side of the islands consists of a narrow shelf, ranging a few hundred metres away from the coast encompassing steep scarps around 100 m high [25].

Two beaches located along the western side of the Maltese Islands are Golden Bay and Għajn Tuffieħa Bay (Figure 1). Golden Bay epitomises a typical Maltese sandy embayment as it is found at a bottom of a valley. This is a pocket beach and experiences sediment runoff from the surrounding natural regions. The sandy beach is composed mainly of pale yellow-brown sand derived from the Globigerina Limestone-dominated cliffs [26].

Located between Ras il-Waħx in the north and the Ġhajj Tuffieħa headland in the south, this beach stretches approximately over 200 m and varies in width between 25 m and 100 m. Ġhajj Tuffieħa Bay (Riviera) is composed of a pocket beach situated between two high rocky headlands, the Ġhajj Tuffieħa headland and the Qarraba headland, along Malta's northwestern coast. This area experiences vigorous waves coming from the west and northwest which erode the base of the coastal slopes consequently resulting in mass movement processes and slope forms leading to sediment movement [27]. Riviera beach is 300 m in length and has a maximum width of 25 m and is composed mainly of pale orange-brown medium sand with gravel towards the south. The beach sediment is mostly derived from the Upper Coralline Limestone erosion of the flanking headlands as well as erosion from the mudslide toes behind the beach [27]. These two beaches have been chosen as both experience similar anthropogenic activities as well as natural process such as sediment transport, due to both being closed pocket beaches situated along the northwestern coast of Malta. This paper aims to make use of several bathymetric mapping techniques to understand the bathymetric profile of these two pocket beaches during differing times of the year.

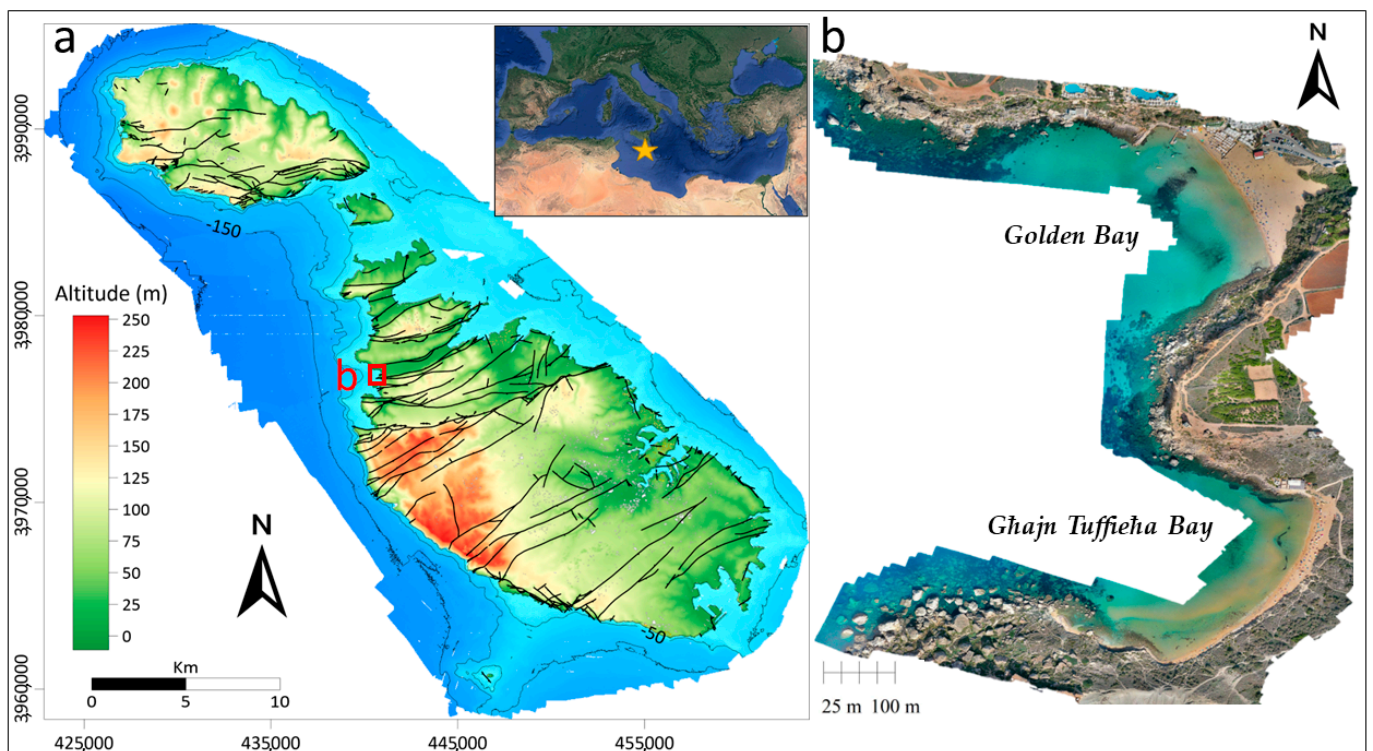


Figure 1. (a) Topo-bathymetric map of the Maltese archipelago showing the main structural lineaments. In the inset, Malta's location in the Mediterranean is highlighted with a star. The red rectangle indicates the position of the studied bays and image "b". (b) orthomosaic of the study area generated by UAV photogrammetry.

2. DataSets

2.1. Satellite Data

In this study, the twin polar-orbiting satellites Sentinel-2A and Sentinel-2B were used [5]. These satellites were developed by the European Space Agency for the Copernicus programme, with each satellite having a revisit period of 10-days. Due to the availability and revisit time of the two satellites, each area is regularly covered every 5-days, with the onboard instruments having the same viewing conditions [28]. The twin satellites carry the Multi-Spectral Instrument (MSI), with a radiometric resolution of 12-bit, giving the satellites a higher capability of detecting differences between reflectance or intensity of the different structures [28]. When compared to Landsat 8, the Sentinel-2 satellites produce an

overall higher accuracy, better results, and a spatial resolution of 10 m [29]. The Sentinel-2 constellation can also measure more spectral bands relative to Landsat 8, producing a clearer, distinct image classification [30].

Sentinel-2 data for the Golden Bay and Ghajn Tuffieħa coastal areas was downloaded through a code implemented within Google Earth Engine (GEE). The downloaded GeoTIFF files corresponded to Level-1C (L1C) products with each radiometric measurement being corrected to Top of Atmosphere (TOA) reflectance. GEE is a cloud-based geographical information analysis system [31], which makes use of a cloud storage system containing a vast catalogue of satellite imagery and several other geospatial data produced in an analysis-ready format [32]. This made GEE optimal for this study as it allowed data to be extracted over the required domain rather than having to download an entire scene as provided by the Copernicus data hub. The GEE script allowed the fusion of data collected over seven consecutive days to obtain a gap-free product. Three files representing measurements from 7 July 2020 to 13 July 2020, from 17 August 2020 to 24 August 2020, and from 19 February 2021 to 25 February 2021, were downloaded. A buffer of three days from the date in which the in situ measurements were captured was applied in order to generate averaged raster sets with reduced cloud coverage, surface reflectance, and any other variable that might have hindered the satellite image quality.

2.2. In Situ Data

For the very nearshore coastal area up to depths of 100 m, where dynamic sediment transport was expected to alter the bathymetry regularly, in situ bathymetric data were collected via the PowerDolphin, a remote surface vehicle (RSV) manufactured by PowerVision [33]. This instrument is a surface water drone which works with PowerSeeker to automatically scan the specified waters and produce bathymetric maps containing accurate underwater information shown in both a visual and digital manner [34]. Moreover, depth values further offshore were obtained from the lidar survey carried out by the Malta Planning Authority in 2018 [35]. This dataset was only used for regions with depths between 10 m and 35 m. Although the measurements were taken a few years prior to this study, due to the nature of the seabed, the values are assumed to have remained constant. Obtaining data from two different in situ techniques were essential to cover the entire region of interest.

Through the use of GIS software, a subset of the in situ data collected by the PowerDolphin and by the lidar data was grouped to obtain points spread over the satellite image (Figure 2).

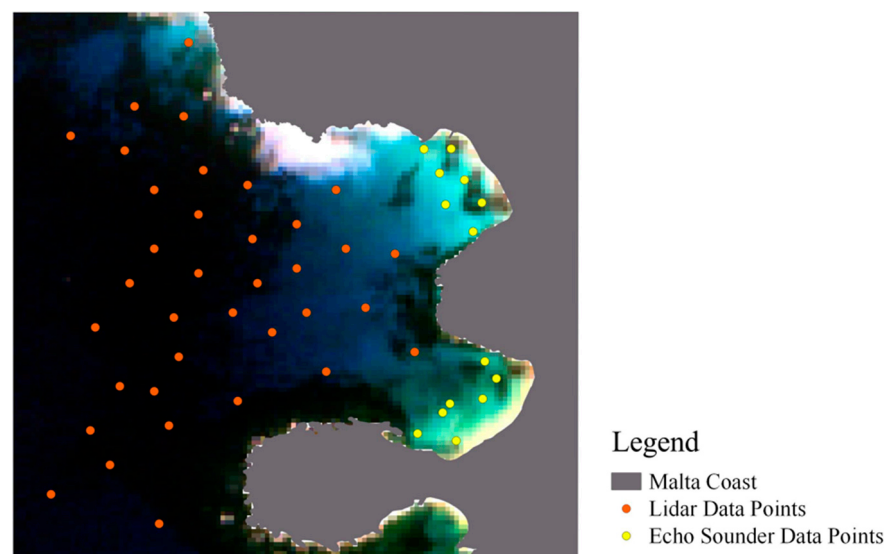


Figure 2. In-situ data points obtained by lidar and sonar techniques.

3. Methods

The intensity values of the ten spectral bands shown in Table 1 were extracted for each in situ vector point. The method proposed by [36] for deriving bathymetry from satellite imagery, which is based on a nonlinear solution and utilises band ratio calculations, was then used to compute the depth values. This method relies on the fact that the reflectance of two bands decrease exponentially with increasing depth [10]. The band with the shorter wavelength will attenuate less than the band with the longer wavelength. Thus, the ratio between the water reflectance values of the spectral bands should increase with depth [37]. Furthermore, this model reduces the effects caused by the dynamic substrate albedo in deriving accurate bathymetric data [2]. Changes in bottom albedo alters both band ratios, respectively, making the ratio substantially more sensitive to variations in depth rather than bottom albedo fluctuations [38]. When compared to the model presented by Lyzenga [39], this solution reduces the sensitivity to bottom changes and requires fewer empirical parameters to predict depth values. Most examples in the literature use the blue (490 nm) and the green (560 nm) wavelengths. However, in this study, to further investigate the best technique for SDB around the Maltese Islands, four other ratios were considered. These included the red wavelength (665 nm) and the infrared wavelength (842 nm). Such bands were chosen as they all have the same spatial resolution of 10 m. The empirical ratio model [36] is expressed by Equations (1) and (2).

$$SDB = m_1 (pSDB) - m_0 \quad (1)$$

$$pSDB = \frac{\ln(nR_w(\lambda_i))}{\ln(nR_w(\lambda_j))} \quad (2)$$

Table 1. Spatial and spectral characteristics of the Sentinel-2 bands used in this study.

Sentinel-2 Bands	Central Wavelength (nm)	Resolution (m)
Band 2—Blue	490	10
Band 3—Green	560	10
Band 4—Red	665	10
Band 5—Vegetation Red Edge	705	20
Band 6—Vegetation Red Edge	740	20
Band 7—Vegetation Red Edge	783	20
Band 8—Near Infrared	842	10
Band 8A—Vegetation Red Edge	865	20
Band 11—Shortwave Infrared	1610	20
Band 12—Shortwave Infrared	2190	20

Here, *SDB* is the Satellite-Derived Bathymetry in metres; *pSDB* is the dimensionless pseudo depth provided by the satellite. The constant *n* is fixed to 1000 to assure the logarithmic ratio with depth results in a linear response and that the ratio remains positive for all points. $R_w(\lambda_i)$ and $R_w(\lambda_j)$ are the water reflectance values for spectral bands *i* and *j*, respectively. The scaling coefficient, m_1 , and the offset coefficient, m_0 , are derived through linear regression of the band ratios from a single satellite.

Apart from generating the *SDB* values using traditional regression techniques, the applicability of machine learning methods was also investigated. A training set was generated from the raw band digital numbers and computed band ratios. The in situ depth measurements from the Golden Bay and the Ghajn Tuffieħa embayments were used as the target values. Random forest, k-star, linear regression, and multilayer perceptron were used to build the models.

Random forest (RF) is a machine learning technique that aggregates a large number of decision trees by sampling the dataset, randomly selects features of each subset to estimate the decision tree, and finally fuses the predicted outputs of each decision tree to enhance the accuracy of the modelled prediction [11]. The user must define two parameters to initialise

the RF algorithm, the number of trees to grow, N , and the number of variables used to split each node, m . Firstly, from 2/3 of the training dataset, N bootstrap samples, which are a smaller sample taken from a larger sample, are drawn while the remaining 1/3 of the training dataset is used to test the error of the predictions [40]. Each bootstrap sample is then used to create an unpruned tree where the best split is determined by randomly selecting m predictors as a subset of the predictor variables at each node. Unlike linear models, RFs have the advantage of accounting for non-linear interactions between variables and can also adapt to process both numerical and categorical data [41]. In comparison to prior straightforward empirical or semi-empirical models, RFs can develop more adaptable and precise models based on existing data [42].

The K-star (K^*) algorithm is an Instance-Based Classifier (IBC). By selecting one transformation at random from all possible transformations, the K^* algorithm utilises an entropic metric based on the probability of changing one instance into another [43]. Therefore, this algorithm varies from other instance-based learners as it makes use of an entropy-based distance function [44]. IBC employ a classification approach that involves comparing an instance to a pre-classified database of examples. The underlying assumption is that instances that are similar to each other will have corresponding classifications. The distance function and the classification function are the two principal components that constitute IBC [44]. The distance function calculates the extent of similarity between two instances, whilst the classification function describes the way in which similarities between instances are utilised to arrive at a final classification for a new instance. Essentially, the distance between instances reflects the level of complexity involved in transforming one instance into another [45].

Linear regression (LR) is the simplest form of regression. The LR algorithm attempts to fit a straight line to the dataset. However, this is only plausible when the variables of the dataset are linear [46]. An advantage that the LR algorithm has over other techniques is that it is simple to gauge and is also easy to bypass overfitting by regularisation. Nonetheless, this machine learning algorithm is not recommended for the more practical applications as it oversimplifies real world situations [46]. LR is tasked to predict a dependent variable value based on a given independent variable and finding out a linear relationship between the input and the output in the process. The regression line of the model is the line of best fit thus, reducing the error difference between the true value and the predicted value to a minimum [47].

Multilayer perceptron (MLP) is a feedforward neural network with one or more layers between the input and output layer [48]. The attributes measured for each training tuple correspond to the inputs towards the network. The inputs are transferred into the input layer and are weighted and fed together to a second neuron-like unit layer, labelled as the hidden layer. Additionally, the output of the hidden layer unit can be inputted into another hidden layer, repeating the process [49]. The MLP can mimic any continuous measurable function between the input and output vectors through the selection of appropriate training data and transfer functions [50]. Furthermore, this algorithm is capable of acquiring knowledge in a supervised manner through training that necessitates the provision of a training dataset consisting of inputs and their corresponding output vectors. The MLP is exposed to the training dataset multiple times, with the network's data being adjusted until the desired input–output correlation is attained [51].

The four techniques were trained and tested on the generated dataset. This provided an indication on the error of the predicted values in comparison to the actual depth values. Four graphs of the actual in situ values against the predicted values by each of the tested models were produced, and the correlation coefficient was computed as an error metric. The models were then applied to all cells over the regions of interest to render bathymetry charts. The outputs were interpolated using the nearest neighbour technique to obtain complete maps.

4. Results

4.1. Għajn Tuffieħa and Golden Bay Embayments

Three images of the regions of interest were selected under cloud-free conditions obtained on 9 July 2020, 20 August 2020, and 22 February 2021 for the Golden Bay embayment and on 10 July 2020, 21 August 2020, and 22 February 2021 for the Għajn Tuffieħa embayment. The in situ data points collected during the same month were coupled together to create three datasets for July 2020, August 2020, and February 2021.

4.2. Correlation Coefficient

The datasets for each month with the in situ depth values together with the band ratios were processed to obtain depth values by each model and, subsequently, a measure of accuracy. In particular, the correlation coefficient was used to measure the performance. The results are presented in Table 2. RF proved to have the best correlation coefficient in all three months, while the other three algorithms, namely, the MLP, K*, and LR, all varied throughout the months.

Table 2. Correlation coefficient of each machine learning algorithm.

Month	Machine Learning Algorithm	Correlation Coefficient
July 2020	Random Forest	0.88
	Multilayer Perceptron	0.77
	K-Star	0.80
	Linear Regression	0.82
August 2020	Random Forest	0.89
	Multilayer Perceptron	0.85
	K-Star	0.81
	Linear Regression	0.80
February 2021	Random Forest	0.94
	Multilayer Perceptron	0.75
	K-Star	0.94
	Linear Regression	0.86

4.3. Predicted Depth Accuracy

Each machine learning algorithm was applied to three separate datasets obtained during the months of July 2020, August 2020, and February 2021. Scatter plots to visualise the correlation between the predicted values of each machine learning algorithm and the in situ depths are presented in Figures 3–5. The regression line corresponds to the relationship between the SDB and the in-situ data, depicting the line of best fit for the data provided.

For the month of July 2020, K* gave the best results, while the LR algorithm attained the least accurate values. Furthermore, MLP delivered inaccurate prediction at the shallowest depths (Figure 3). For August 2020, the predicted depth values of each algorithm were more accurate than the July 2020 depth values as all four scatter plots displayed a higher positive correlation with the regression line (Figure 4). K* and LR were still the most and least accurate algorithms, respectively. RF and MLP both exhibit an accurate positive correlation, and both produced good results similar to those by K*. The results predicted for February 2021 followed similar trends as the months of July and August 2020, albeit with a higher accuracy (Figure 5). K*, RF, and MLP produced the most accurate depths while the LR algorithm resulted in a weaker relationship between the predicted and in situ depth values. In general, K* proved to be the best-fitting algorithm out of the four algorithms. This was followed by the RF algorithm, which also outperformed MLP and LR.

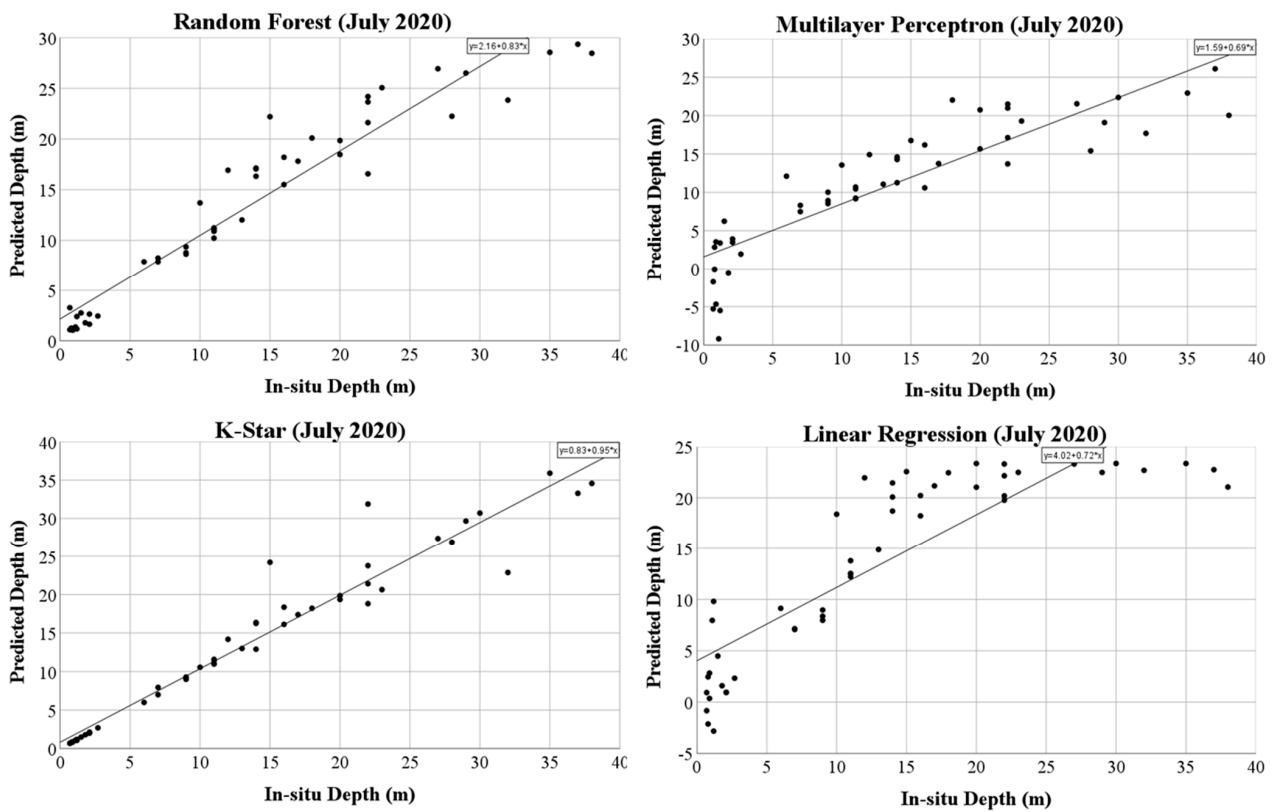


Figure 3. Scatter plots displaying the accuracy of the predicted depth values compared to the in situ depth values for the month of July 2020.

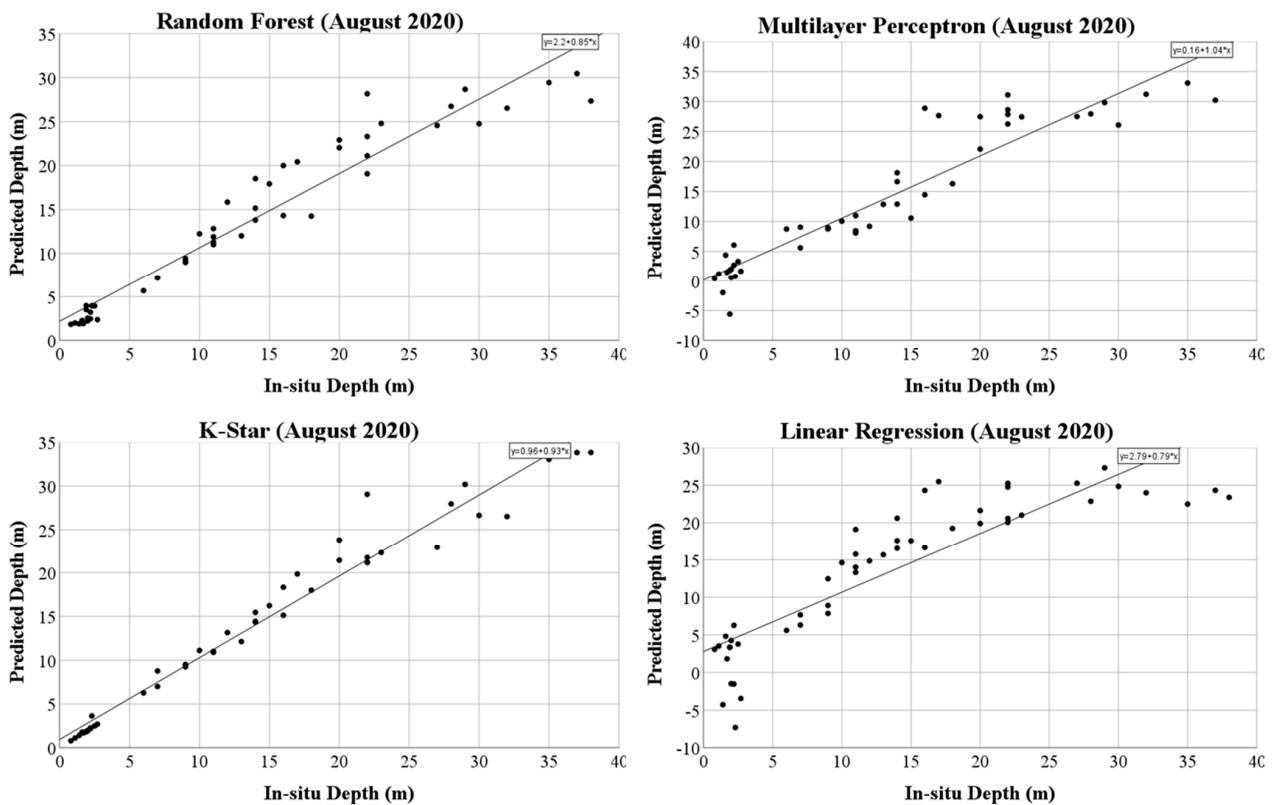


Figure 4. Scatter plots displaying the accuracy of the predicted depth values compared to the in situ depth values for the month of August 2020.

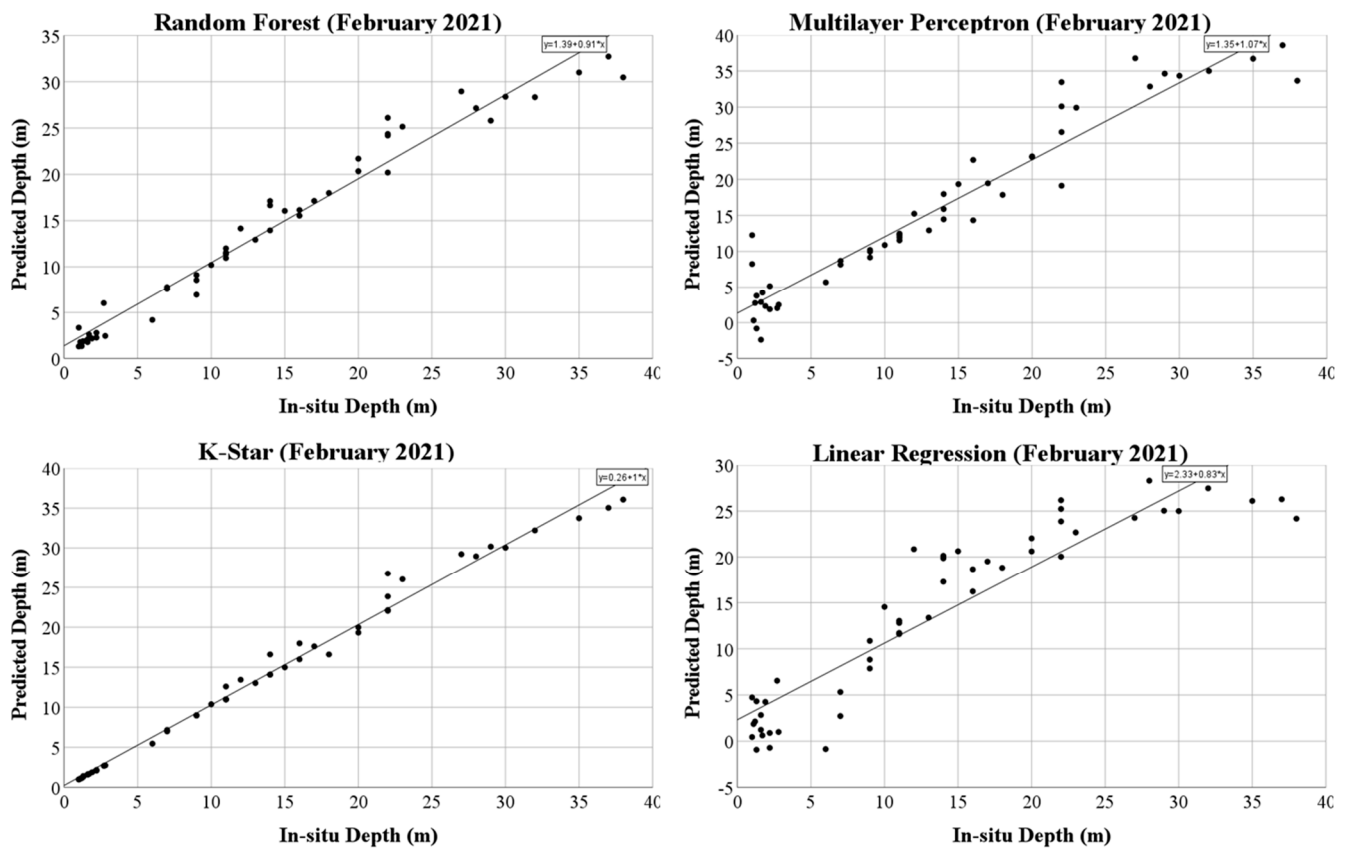


Figure 5. Scatter plots displaying the accuracy of the predicted depth values compared to the in situ depth values for the month of February 2021.

4.4. SDB Maps

Four maps were produced for each date in order to have a visual representation of how the predicted depth values of the four separate machine learning algorithms vary as one moves away from the coastline and during different months of the year. These are shown in Figures 6–8.

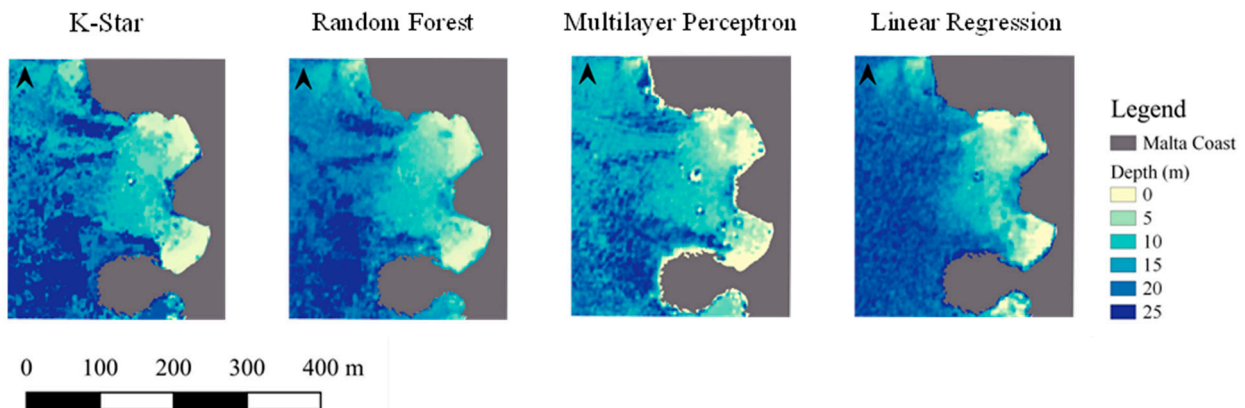


Figure 6. SDB maps for the month of July 2020.

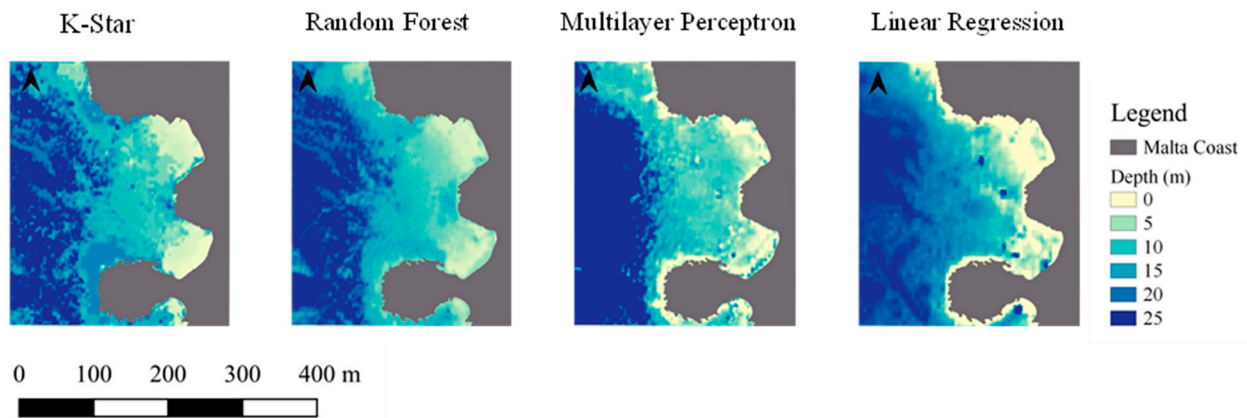


Figure 7. SDB maps for the month of August 2020.

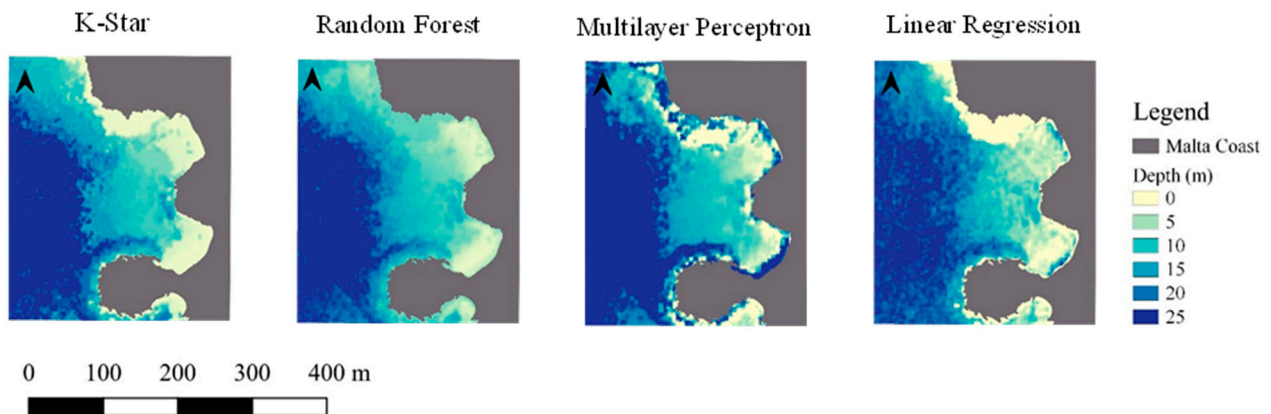


Figure 8. SDB maps for the month of February 2021.

The computed bathymetry of Golden Bay and Ghajn Tuffieħa Bay displayed noticeable variations from July 2020 to February 2021 as evident from Figures 6–8. The initial data collected in July 2020 indicated the presence of shallower waters even at locations away from the shore. Furthermore, there was a slight alteration in the bathymetry between July and August 2020, with deeper depths observed further offshore but with some shallow areas still visible. Comparing the February 2021 maps with those of August 2020 revealed a clear increase in bathymetric depth further offshore with a gradual transition from shallow depths situated close to the shore to deeper depths further offshore.

The observed bathymetric changes may be the result of various processes. Sediment runoff could be one of the primary causes of bathymetric changes particularly those near the coastline. This is because both Ghajn Tuffieħa Bay and Golden Bay are pocket beaches that are surrounded by natural vegetated regions and globigerina limestone headlands, which are highly susceptible to erosion caused by wave action. Additionally, during the six-month period, seasonal changes between summer and winter could have also contributed to the bathymetric changes further offshore. Storm surges and large waves could have also occurred between August 2020 and February 2021, causing sediment movement and seabed erosion, significantly impacting the offshore waters and consequently influencing the water depth.

5. Concluding Remarks

The main aim of this study was to combine and integrate three separate bathymetric data collection techniques including sonar, lidar, and SDB to produce high resolution bathymetric maps of the Ghajn Tuffieħa and Golden Bay region. Through the use of GEE, Sentinel-2 data, and in situ data, an empirical pre-processing workflow for estimating SDB

was developed. The results obtained by four different machine learning techniques were also compared. Different depth accuracies were produced by each algorithm with K* and Random Forest delivering the most accurate depth values and LR having the least accurate depth values over the entire three-month study period.

This study was possible due to the use of the PowerDolphin which provided in situ bathymetric data at very shallow depths. This instrument covers a wide range of applications due to its sonar technology, which gives quick feedback on the underwater dynamics, including the topographical distribution of the seabed and fish distribution. Thus, it can be used for both scientific research as well as a tool for professional fishermen. The PowerDolphin is a relatively cheap and time-effective tool to create bathymetric maps needed for coastal management, environmental impact assessments, and seasonal sediment monitoring. Furthermore, this equipment improves the results of shallow bathymetric surveys due to its practicality and high-resolution output.

With these new advances in submarine topographic mapping, it has become possible to frequently update bathymetric maps, leading in turn to several advantages. Most importantly, due to the constant anthropogenic pressures experienced by coastal zones, the evolution of such regions can be mapped to help better understand the impacts exerted on these transitional zones by human activities such as dredging and coastal armouring and to help predict future coastal morphodynamics as a way of mitigating the same putative impacts. Furthermore, accurate, up-to-date, high-resolution bathymetric information can also be crucial for navigation and Environment Impact Assessment (EIA) processes, specifically within nautical charts, benthic mapping, risk assessments, sea-level changes, tsunami modelling, and sediment transport.

The integration of SDB data in coastal management presents several benefits to coastal geomorphologists and managers. The utilisation of satellite images enables extensive coverage and can be used to record bathymetric data over vast regions, resulting in a more time-efficient data acquisition approach when compared to in situ measurements.

Once the technique has been calibrated for each site, the ability to estimate bathymetric data using SDB can lead to the generation of bathymetric maps with a temporal resolution determined by the satellite revisit time, usually a few days, depending on the satellite. This can provide more up-to-date data, compared to relying solely on in situ acquisitions, which are typically more costly and less frequent in time. Additionally, previous satellite imagery can be utilised to estimate bathymetry from past time periods. The extraction of bathymetry from satellite images acquired over time can be used to comprehend temporal changes in sedimentation patterns that shape the seafloor in coastal systems. This information is particularly valuable for research on coastal erosion and sedimentation and can result in morphodynamic models that provide managers with a tool capable of predicting the dynamic evolution of coastal sediment and make informed management decisions [52–54].

Author Contributions: Conceptualisation, A.G.; methodology, A.G.; software, G.D. formal analysis, G.D.; writing—original draft preparation, G.D.; writing—review and editing, A.G., A.D., S.D.; visualisation, L.G.; supervision, A.G., S.D.; project administration, S.D., L.G.; funding acquisition, S.D. All authors have read and agreed to the published version of the manuscript.

Funding: This research was supported by the project Satellite Investigation to study Pocket BEach Dynamics (SIPOBED, SRF-2021-2S1, PI: Sebastiano D’Amico), financed by the Malta Council for Science and Technology (MCST, <https://mcst.gov.mt/>, accessed on 5 April 2023) through the Space Research Fund (Building capacity in the downstream Earth Observation Sector) a programme supported by the European Space Agency.

Institutional Review Board Statement: Not applicable.

Informed Consent Statement: Not applicable.

Data Availability Statement: All data are available upon request.

Acknowledgments: The authors thank Planning Authority for providing ERDF 156 data, Developing National Environmental Monitoring Infrastructure and Capacity, Malta Environment & Planning Authority, 2013. The authors would also like to thank Hiba Zakie for providing the in-situ depth values measured by the PowerVision PowerDolphin.

Conflicts of Interest: The authors declare no conflict of interest.

References

- Dierssen, H.M.; Theberge, A.E. Bathymetry: Assessing Methods. *Encycl. Nat. Resour.* **2014**, *2*, 1–8.
- Jawak, S.D.; Vadlamani, S.S.; Luis, A.J. A synoptic review on deriving bathymetry information using remote sensing technologies: Models, methods and comparisons. *Adv. Remote Sens.* **2015**, *4*, 147. [\[CrossRef\]](#)
- Weatherall, P.; Marks, K.M.; Jakobsson, M.; Schmitt, T.; Tani, S.; Arndt, J.E.; Rovere, M.; Chayes, D.; Ferrini, V.; Wigley, R. A new digital bathymetric model of the world's oceans. *Earth Space Sci.* **2015**, *2*, 331–345. [\[CrossRef\]](#)
- Traganos, D.; Poursanidis, D.; Aggarwal, B.; Chrysoulakis, N.; Reinartz, P. Estimating satellite-derived bathymetry (SDB) with the google earth engine and sentinel-2. *Remote Sens.* **2018**, *10*, 859. [\[CrossRef\]](#)
- Gao, J. Bathymetric mapping by means of remote sensing: Methods, accuracy and limitations. *Prog. Phys. Geogr.* **2009**, *33*, 103–116. [\[CrossRef\]](#)
- Caballero, I.; Stumpf, R.P. Retrieval of nearshore bathymetry from Sentinel-2A and 2B satellites in South Florida coastal waters. *Estuar. Coast. Shelf Sci.* **2019**, *226*, 106277. [\[CrossRef\]](#)
- D'Amico, S.; Galone, L.; Colica, E.; Gauci, A.; Valentino, G.; Piroddi, L.; Iregbeyen, P. Investigating Pocket beach dynamics in Malta: The SIPOBED project. In Proceedings of the IEEE International Workshop on Metrology for the Sea; Learning to Measure Sea Health Parameters (MetroSea), Milazzo, Italy, 3–5 October 2022; pp. 497–500.
- Muzirafuti, A.; Barreca, G.; Crupi, A.; Faina, G.; Paltrinieri, D.; Lanza, S.; Randazzo, G. The contribution of multispectral satellite image to shallow water bathymetry mapping on the Coast of Misano Adriatico, Italy. *J. Mar. Sci. Eng.* **2020**, *8*, 126. [\[CrossRef\]](#)
- Cesbron, G.; Melet, A.; Almar, R.; Lifermann, A.; Tullo, D.; Crosnier, L. Pan-European Satellite-Derived Coastal Bathymetry—Review, User Needs and Future Services. *Front. Mar. Sci.* **2021**, *8*, 740830. [\[CrossRef\]](#)
- Amrari, S.; Bourassin, E.; Andréfouët, S.; Soulard, B.; Lemonnier, H.; Le Gendre, R. Shallow water bathymetry retrieval using a band-optimization iterative approach: Application to New Caledonia coral reef lagoons using Sentinel-2 data. *Remote Sens.* **2021**, *13*, 4108. [\[CrossRef\]](#)
- Duan, Z.; Chu, S.; Cheng, L.; Ji, C.; Li, M.; Shen, W. Satellite-derived bathymetry using Landsat-8 and Sentinel-2A images: Assessment of atmospheric correction algorithms and depth derivation models in shallow waters. *Opt. Express* **2022**, *30*, 3238–3261. [\[CrossRef\]](#)
- Misra, A.; Ramakrishnan, B. Assessment of coastal geomorphological changes using multi-temporal Satellite-Derived Bathymetry. *Cont. Shelf Res.* **2020**, *207*, 104213. [\[CrossRef\]](#)
- Janowski, L.; Trzcinska, K.; Tegowski, J.; Kruss, A.; Rucinska-Zjadacz, M.; Pocwiardowski, P. Nearshore Benthic Habitat Mapping Based on Multi-Frequency, Multibeam Echosounder Data Using a Combined Object-Based Approach: A Case Study from the Rowy Site in the Southern Baltic Sea. *Remote Sens.* **2018**, *10*, 1983. [\[CrossRef\]](#)
- Thierry, S.; Dick, S.; George, S.; Benoit, L.; Cyrille, P. EMODnet Bathymetry a Compilation of Bathymetric Data in the European Waters. In *OCEANS 2019—Marseille*; IEEE: Toulouse, France, 2019.
- Kutser, T.; Hedley, J.; Giardino, C.; Roelfsema, C.; Brando, V.E. Remote Sensing of Shallow Waters—A 50 Year Retrospective and Future Directions. *Remote Sens. Environ.* **2020**, *240*, 111619. [\[CrossRef\]](#)
- Guo, Q.; Wenkai, L.; Hong, Y.; Otto, A. Effects of Topographic Variability and Lidar Sampling Density on Several DEM Interpolation Methods. *Photogramm. Eng. Remote Sens.* **2010**, *76*, 701–712. [\[CrossRef\]](#)
- Chirayath, V.; Earle, S.A. Drones That See through Waves—Preliminary Results from Airborne Fluid Lensing for Centimetre-Scale Aquatic Conservation. *Aquat. Conserv. Mar. Freshw. Ecosyst.* **2016**, *26*, 237–250. [\[CrossRef\]](#)
- Figueiredo, I.N.; Pinto, L.; Goncalves, G. A Modified Lyzenga's Model for Multispectral Bathymetry Using Tikhonov Regularization. *IEEE Geosci. Remote Sens. Lett.* **2016**, *13*, 53–57. [\[CrossRef\]](#)
- Hogrefe, K.R.; Wright, D.J.; Hochberg, E.J. Derivation and Integration of Shallow-Water Bathymetry: Implications for Coastal Terrain Modeling and Subsequent Analyses. *Mar. Geod.* **2008**, *31*, 299–317. [\[CrossRef\]](#)
- Giordan, D.; Notti, D.; Villa, A.; Zucca, F.; Calò, F.; Pepe, A.; Dutto, F.; Pari, P.; Baldo, M.; Allasia, P. Low Cost, Multiscale and Multi-Sensor Application for Flooded Area Mapping. *Nat. Hazards Earth Syst. Sci.* **2018**, *18*, 1493–1516. [\[CrossRef\]](#)
- Hodúl, M.; Bird, S.; Knudby, A.; Chénier, R. Satellite Derived Photogrammetric Bathymetry. *ISPRS J. Photogramm. Remote Sens.* **2018**, *142*, 268–277. [\[CrossRef\]](#)
- Wazaz, H.; Deidun, A.; Gauci, A. Use of a low-cost unmanned surface vessel for bathymetry surveys and pocket beach sediment dynamics monitoring. In Proceedings of the IEEE International Workshop on Metrology for the Sea; Learning to Measure Sea Health Parameters (MetroSea), Milazzo, Italy, 3–5 October 2022; pp. 488–492.
- Thomas, N.; Pertiwi, A.P.; Traganos, D.; Lagomasino, D.; Poursanidis, D.; Moreno, S.; Fatoyinbo, L. Space-Borne Cloud-Native Satellite-Derived Bathymetry (SDB) Models Using ICESat-2 and Sentinel-2. *Geophys. Res. Lett.* **2021**, *48*, e2020GL092170. [\[CrossRef\]](#)

24. French, C.; Hunt, C.; Grima, R.; McLaughlin, R.; Stoddart, S.; Malone, C. Temple Landscapes: Fragility, change and resilience of Holocene environments in the Maltese Islands. In *McDonald Institute for Archaeological Research Cambridge*; Queen's University Belfast: Belfast, UK, 2020.
25. Illies, J.H. Graben formation—The Maltese Islands—A case history. *Dev. Geotecton.* **1981**, *17*, 151–168.
26. Prampolini, M.; Coratza, P.; Rossi, S.; Parenti, C.; Galea, C.; Caruana, A.; Soldati, M. Geomorphology of the seafloor north east of the Maltese Islands, Central Mediterranean. *J. Maps* **2021**, *17*, 465–475. [[CrossRef](#)]
27. Farrugia, M.T. Coastal erosion along northern Malta: Geomorphological processes and risks. *Geogr. Fis. Dinam. Quat.* **2008**, *31*, 149–160.
28. Zammit Pace, M.L.; Bray, M.; Potts, J.; Baily, B. The Beaches of the Maltese Islands: A Valuable but Threatened Resource? In *World Geomorphological Landscapes*; Springer: Berlin/Heidelberg, Germany, 2019; pp. 213–227.
29. ESA. European Space Agency. Available online: <https://www.esa.int/> (accessed on 13 September 2022).
30. Sibanda, M.; Mutanga, O.; Rouget, M. Discriminating Rangeland Management Practices Using Simulated HypsIRI, Landsat 8 OLI, Sentinel 2 MSI, and VEN μ S Spectral Data. *IEEE J. Sel. Top. Appl. Earth Obs. Remote Sens.* **2016**, *9*, 3957–3969. [[CrossRef](#)]
31. Forkuor, G.; Dimobe, K.; Serme, I.; Tondoh, J.E. Landsat-8 vs. Sentinel-2: Examining the Added Value of Sentinel-2's Red-Edge Bands to Land-Use and Land-Cover Mapping in Burkina Faso. *GIScience Remote Sens.* **2017**, *55*, 331–354. [[CrossRef](#)]
32. Sagawa, T.; Yamashita, Y.; Okumura, T.; Yamanokuchi, T. Satellite Derived Bathymetry Using Machine Learning and Multi-Temporal Satellite Images. *Remote Sens.* **2019**, *11*, 1155. [[CrossRef](#)]
33. Earthengine, Google Earth Engine. Available online: <https://earthengine.google.com/> (accessed on 14 September 2022).
34. Powervision, PowerVision. Available online: <https://www.powervision.me/en/> (accessed on 14 September 2022).
35. *ERDF 156 data*; Developing National Environmental Monitoring Infrastructure and Capacity. Malta Environment & Planning Authority: Floriana, Malta, 2013.
36. Stumpf, R.P.; Holderied, K.; Sinclair, M. Determination of Water Depth with High-Resolution Satellite Imagery over Variable Bottom Types. *Limnol. Oceanogr.* **2003**, *48*, 547–556. [[CrossRef](#)]
37. Vargas, R.; Wasserman, J.C.d.F.A.; da Silva, A.L.; Tavares, T.L.; dos Santos, C.A.; Dias, F.F. Satellite-Derived Bathymetry Models from Sentinel-2A and 2B in the Coastal Clear Waters of Arraial Do Cabo, Rio de Janeiro, Brazil. *Rev. Bras. Geogr. Fis.* **2021**, *14*, 3078. [[CrossRef](#)]
38. Philpot, W.D. Bathymetric Mapping with Passive Multispectral Imagery. *Appl. Opt.* **1989**, *28*, 1569. [[CrossRef](#)]
39. Lyzenga, D.R. Passive Remote Sensing Techniques for Mapping Water Depth and Bottom Features. *Appl. Opt.* **1978**, *17*, 379. [[CrossRef](#)] [[PubMed](#)]
40. Akar, Ö.; Güngör, O. Classification of Multispectral Images Using Random Forest Algorithm. *J. Geod. Geoinf.* **2012**, *1*, 105–112. [[CrossRef](#)]
41. Yunus, A.P.; Dou, J.; Song, X.; Avtar, R. Improved Bathymetric Mapping of Coastal and Lake Environments Using Sentinel-2 and Landsat-8 Images. *Sensors* **2019**, *19*, 2788. [[CrossRef](#)]
42. Manessa, M.D.M.; Kanno, A.; Sekine, M.; Haidar, M.; Yamamoto, K.; Imai, T.; Higuchi, T. Satellite-Derived Bathymetry Using Random Forest Algorithm and Worldview-2 Imagery. *Geoplan. J. Geomat. Plan.* **2016**, *3*, 117. [[CrossRef](#)]
43. Madhusudana, C.K.; Kumar, H.; Narendranath, S. Condition Monitoring of Face Milling Tool Using K-Star Algorithm and Histogram Features of Vibration Signal. *Eng. Sci. Technol. Int. J.* **2016**, *19*, 1543–1551. [[CrossRef](#)]
44. Cleary, J.G.; Trigg, L.E. K*: An Instance-Based Learner Using an Entropic Distance Measure. *Mach. Learn. Proc.* **1995**, 1995, 108–114.
45. Mahmood, D.Y.; Hussein, M.A. Intrusion Detection System Based on K-Star Classifier and Feature Set Reduction. *IOSR J. Comput. Eng.* **2013**, *15*, 107–112.
46. ML | Linear Regression. Available online: <https://www.geeksforgeeks.org/ml-linear-regression/#:~:text=Linear%20Regression%20is%20a%20machine> (accessed on 9 October 2022).
47. Ray, S. A Quick Review of Machine Learning Algorithms. In Proceedings of the 2019 International Conference on Machine Learning, Big Data, Cloud and Parallel Computing (COMITCon), Faridabad, India, 14–16 February 2019.
48. Kumar, Y.; Sahoo, G. Analysis of Parametric & Non Parametric Classifiers for Classification Technique Using WEKA. *Int. J. Inf. Technol. Comput. Sci.* **2012**, *4*, 43–49.
49. Arora, R.; Suman, S. Comparative Analysis of Classification Algorithms on Different Datasets Using WEKA. *Int. J. Comput. Appl.* **2012**, *54*, 21–25. [[CrossRef](#)]
50. Hornik, K.; Stinchcombe, M.; White, H. Multilayer Feedforward Networks Are Universal Approximators. *Neural Netw.* **1989**, *2*, 359–366. [[CrossRef](#)]
51. Gardner, M.W.; Dorling, S.R. Artificial Neural Networks (the Multilayer Perceptron)—A Review of Applications in the Atmospheric Sciences. *Atmos. Environ.* **1998**, *32*, 2627–2636. [[CrossRef](#)]
52. Randazzo, G.; Italiano, F.; Micallef, A.; Tomasello, A.; Cassetti, F.P.; Zammit, A.; D'Amico, S.; Saliba, O.; Cascio, M.; Cavallaro, F.; et al. WebGIS Implementation for Dynamic Mapping and Visualization of Coastal Geospatial Data: A Case Study of BESS Project. *Appl. Sci.* **2021**, *11*, 8233. [[CrossRef](#)]

53. Román, A.; Tovar-Sánchez, A.; Gauci, A.; Deidun, A.; Caballero, I.; Colica, E.; D'Amico, S.; Navarro, G. Water-Quality Monitoring with a UAV-Mounted Multispectral Camera in Coastal Waters. *Remote Sens.* **2023**, *15*, 237. [[CrossRef](#)]
54. Colica, E.; Galone, L.; D'Amico, S.; Gauci, A.; Iannucci, R.; Martino, S.; Pistillo, D.; Iregbeyen, P.; Valentino, G. Evaluating Characteristics of an Active Coastal Spreading Area Combining Geophysical Data with Satellite, Aerial, and Unmanned Aerial Vehicles Images. *Remote Sens.* **2023**, *15*, 1465. [[CrossRef](#)]

Disclaimer/Publisher's Note: The statements, opinions and data contained in all publications are solely those of the individual author(s) and contributor(s) and not of MDPI and/or the editor(s). MDPI and/or the editor(s) disclaim responsibility for any injury to people or property resulting from any ideas, methods, instructions or products referred to in the content.